PCCP

ROYAL SOCIETY OF CHEMISTRY

PAPER

View Article Online
View Journal | View Issue

Cite this: *Phys. Chem. Chem. Phys.*, 2025, **27**, 20787

Revealing the dominant reactive oxygen species in aqueous amine solutions for carbon capture

Dipam Patel, Jiwon Yu and Gyeong S. Hwang *

Received 9th July 2025,
Accepted 8th September 2025

DOI: 10.1039/d5cp02617b

rsc.li/pccp

Reactive oxygen species (ROS) play a critical role in the oxidative degradation of amine solvents for carbon dioxide (CO_2) capture, resulting in solvent loss and the formation of harmful byproducts. While hydroxyl radicals ($^{\bullet}OH$) or direct oxidation by metal cations have been proposed as potential initiators of the oxidative degradation, the specific ROS involved remains unclear. In this study, we propose that superoxide (O_2^-) may be the dominant ROS under alkaline conditions during CO_2 capture, based on the thermodynamic analysis of reduction reactions. Using quantum mechanical (QM) calculations, we further demonstrate that ferrous iron (Fe^{2+}) complexes, when coordinated to electron-donating ligands such as carbamates and bicarbonates, exhibit significantly lower reduction potentials, making them effective reductants for O_2. The large concentration of these ligands in CO_2-loaded amine solution may allow for the production of such reductive Fe complexes and in turn facilitate O_2 reduction to O_2^-. Finally, we propose a reaction mechanism, supported by molecular dynamics simulations, where O_2^- initiates the decomposition of protonated monoethanolamine. These findings offer new insights into the primary ROS involved in the oxidative degradation of aqueous amines and suggest strategies to mitigate solvent degradation in CO_2 capture processes.

1. Introduction

Chemical absorption of carbon dioxide (CO_2) from post-combustion gases is one of the most promising technologies for mitigating greenhouse gas emissions.[1] However, the degradation of amine solvents and the associated costs of solvent replacement limit widespread implementation of such carbon capture systems.[2] In particular, oxidative degradation of amine solvents leads to substantial solvent depletion, driving up operational costs. It also produces harmful byproducts like ammonia, formic acid, and aldehyde, which can damage equipment and decrease process efficiency.

Oxidative degradation occurs in the presence of O_2 from flue gas and solvated transition metals leached from the absorber walls. Previous studies have assumed two possible mechanisms: direct oxidation of amines by Fe^{3+}[3,4] or *via* the production of hydroxyl radicals ($^{\bullet}OH$).[5] However, the former pathway would produce a highly unstable hydrocarbon radical which is thermodynamically unfavorable without significant potential biasing. Our preliminary calculations support this, showing a standard potential of less than −1.3 V *vs.* SHE for the reduction of ferric iron (Fe^{3+}) coupled with amine oxidation. Furthermore, the low solubility of Fe^{3+} in aqueous systems suggests that the energetic cost for this reaction could be even higher in real systems. Hence, this pathway is highly unlikely to occur without strong chelating agents to modify the environment of Fe^{3+}. The latter mechanism involving the production of $^{\bullet}OH$ is also somewhat dubious, as the generation of $^{\bullet}OH$ from O_2 requires the transfer of 3 electrons and 2–3 protons, depending on pH. This reaction may be readily observed in electrochemical systems with an applied potential and an abundant electron source; however, it is less feasible in aqueous amine-based CO_2 capture systems. In such systems, the electron source is a small quantity (<1 M) of dissolved metal atoms. In addition, oxidative degradation occurs in alkaline conditions due to the presence of amines. This alkaline environment results in a scarcity of protons, which hinders formation of a key ROS intermediate, H_2O_2, as 2 protons must be transferred to O_2. The complex interplay between oxygen species, solvated metal ions, and environmental conditions results in a system where the dominant ROS is not obvious.

In this work, we investigate the dominant ROS in aqueous amine solutions for CO_2 capture. We conduct a comprehensive thermodynamic analysis of the reduction reactions of potential ROS to evaluate their feasibility under typical operating conditions. Additionally, we examine the role of solvated metal ion complexes and the effect of modifying their ligand environment on the reduction processes by employing quantum mechanical (QM) simulations. Also, we propose a mechanism in which superoxide (O_2^-) can initiate the oxidative degradation of monoethanolamine (MEA), a benchmark solvent for CO_2 capture.[6]

McKetta Department of Chemical Engineering, University of Texas at Austin, Austin, Texas 78712, USA. E-mail: gshwang@che.utexas.edu; Fax: +1-512-471-7060; Tel: +1-512-471-4847

2. Computational methods

Density functional theory (DFT) static calculations were performed using the Gaussian16 software package.[7] Fe complex structures were geometry optimized at the B3LYP/6-31+G(d) level of theory.[8] Single point energies were calculated using the M06L functional with a split basis of cc-PVDZ (Fe) and 6-31G+(d,p) (C, H, O, N).[9] A thermodynamic cycle with the SMD solvation model was used to account for solvation effects.[10] These settings have been shown previously to produce very accurate estimates for the redox potentials of $Fe^{2+/3+}$ complexes.[11] The oxidation potentials of amines were calculated using a similar method with the Fe complexes. The CAM-B3LYP functional was used over M06 for its accuracy in amines.[12]

DFT-based *ab initio* molecular dynamics (AIMD) were performed in CPMD.[13] The exchange functional of Becke[14] and the correlation functional of Lee, Yang, and Parr[15] were used as they were employed by previous calculations involving O_2^-.[16,17] Norm-conserving Troullier–Martins pseudopotentials[18] in the nonlocal form of Kleinman and Bylander[19] were used to describe the valence-core electron interaction. A cutoff for the plane-wave basis was set at 45 Ry. The local spin density (LSD) approximation was used to treat the spin-polarized character of the system. A fictitious electron mass of 600 amu and a timestep of 0.12 fs were used to ensure adiabaticity in CPMD. Hydrogen atoms were treated as deuterium to ensure no electronic–ionic coupling. Electronic and ionic dynamics were controlled by a chain of Nose–Hoover thermostats.[20–22] Free-energy sampling was performed using the PLUMED package.[23] The well-tempered metadynamics algorithm was used to sample the free-energy surface.[24,25] Hills with an initial height of 0.94 kcal mol^{-1} and width of 0.1 Å were deposited at a rate of 10^{-2} fs^{-1}. ΔT was set to 4500 K, corresponding to T = 300 K and a damping parameter of 15. Molecular dynamics trajectories were analyzed using the MDAnalysis python library.[26–28]

A static calculation of the transition state for this reaction was performed using the Vienna *ab initio* simulation package (VASP)[29] and the dimer method of Henkelmann.[30] This calculation utilized the generalized gradient approximation (GGA) functional of Perdew, Burke, and Ernzerhof (PBE)[31] and the Projector-Augmented Wave (PAW) method of Kresse.[32]

3. Results and discussion

3.1. Effect of pH on ROS generation

We begin with a simple thermodynamic analysis of ROS generation by using the reduction potentials for the steps of the oxygen reduction reaction (ORR) in aqueous solutions. The three reactions considered, along with their standard reduction potentials, are as follows:[33]

$$O_2 + e^- \rightarrow O_2^-, \quad E^0 = -0.33 \text{ V } \textit{vs.} \text{ SHE} \qquad \text{(R1)}$$

$$O_2^- + 2H^+ + e^- \rightarrow H_2O_2, \quad E^0 = 0.92 \text{ V } \textit{vs.} \text{ SHE} \qquad \text{(R2)}$$

$$H_2O_2 + H^+ + e^- \rightarrow H_2O + {}^\bullet OH, \quad E^0 = 0.32 \text{ V } \textit{vs.} \text{ SHE} \qquad \text{(R3)}$$

As shown in (R1)–(R3), it is assumed that hydroxyl radical ($^\bullet$OH) is the dominant ROS due to the favorable standard reduction potential of the latter steps in comparison to (R1). However, standard potentials are defined at pH = 0 with 1 M concentrations of oxidized and reduced species. The value of the true reduction potential with changing reactant/product concentrations and pH is given by the Nernst equation, rendered below in eqn (1) as that for a general redox reaction, $X_O + \Delta n_H H^+ + ne^- \rightarrow X_R$, where Δn_H denotes the number of protons consumed, the reduction potential E can be corrected to account for both proton and species concentrations, as described in eqn (1). Here, R is gas constant, F is Faraday's constant, T is temperature. For convenience, eqn (1) can be separated into a reductant/oxidant concentration term and a pH term using the definition of pH (pH = $-\log_{10}[H^+]$), as done in eqn (2).

$$E - E^0 = -\frac{RT}{F}\ln\left(\frac{[X_R]}{[X_O]}\frac{1}{[H^+]^{-\Delta n_H}}\right) \qquad (1)$$

$$E - E^0 = -\frac{RT}{F}\ln\left(\frac{[X_R]}{[X_O]}\right) + \frac{RT}{F(\log_{10} e)}\Delta n_H \text{pH} \qquad (2)$$

Using eqn (2), we first show the effect of pH alone on the reduction potentials of each ROS of interest, neglecting concentration effects from the first term. As shown in Fig. 1(a), the reduction potentials of (R2) and (R3) decline significantly with increasing pH, becoming endergonic after pH = 5 and pH = 7, respectively. The requirement of $2H^+$ to form H_2O_2 severely limits its production under alkaline conditions. On the other hand, the reduction potential of (R1) remains unchanged with varying pH as it does not involve protonation. As the pH shifts further toward the alkaline range, the equilibrium potentials of all three reactions become comparable at pH $\approx$ 10, with (R1) becoming the most favorable reaction at higher pH values.

Fig. 1(a) describes ROS generation as a function of pH at a set potential (E) of 0.771 V *vs.* SHE, similar to assuming an abundant electron supply from an electrode. However, in typical CO_2 stripping processes, the electron source is limited to a small concentration of dissolved metal ions. These metals undergo oxidation in the presence of electron acceptors with their own half-cell reactions at certain standard reduction potentials (E_M).

$$M \rightarrow M^+ + e^-, \quad E^0 = E_M \qquad \text{(R4)}$$

To account for metal cation oxidation as the sole source of electrons, we can combine the two half-reactions, reversing (R4), to obtain a standard full cell potential:

$$E^0 = E_R - E_M \qquad (3)$$

We can also write a version of the Nernst equation for the full cell to account for non-standard concentrations:

$$E - (E_R - E_M) = -\frac{RT}{F}\ln\left(\frac{[X_R]}{[X_O]}\frac{[M^+]}{[M]}\right) - \frac{RT}{F(\log_{10} e)}\Delta n_H \text{pH} \qquad (4)$$

Setting E (the driving force) to 0 to correspond to equilibrium, the equation for the equilibrium concentration of species X_O

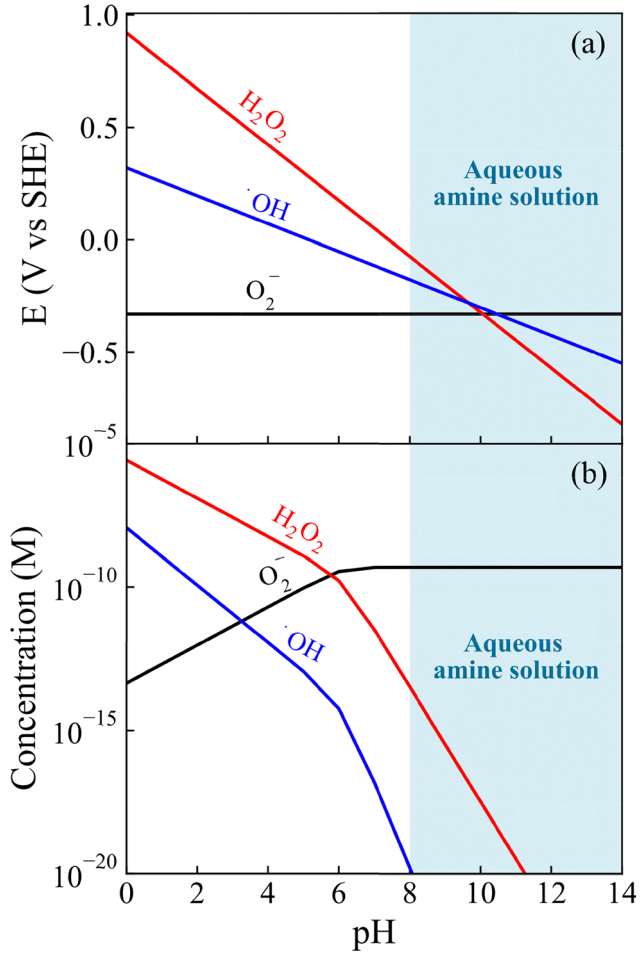

Fig. 1 (a) Calculated equilibrium potentials for O_2 reduction (R1), H_2O_2 formation (R2), and $^{\bullet}OH$ formation (R3) and (b) concentration of ROS at different levels of alkalinity.

becomes:

$$[X_O] = [X_R]\frac{[M^+]}{[M]}e^{\frac{-(E_R-E_M)F}{RT}}e^{\frac{1}{(\log_{10} e)}\Delta n_H pH} \quad (5)$$

Defining eqn (5) for each reaction (R1)–(R3) gives a system of equations with unknown concentrations of 5 species (M, M^+, O_2^-, H_2O_2, $^{\bullet}OH$), assuming constant H^+, O_2, and H_2O concentrations. An additional two balances are required to fully define the system.

$$[M] = [M]_0 - [O_2^-] - 2[H_2O_2] - 3[^{\bullet}OH] \quad (6)$$

$$[M]_0 = [M] + [M^+] \quad (7)$$

Eqn (6) is a balance on electrons, as the metal is the only source, and eqn (7) is a balance on the total metal species concentration. Finally, we also specify a temperature of 313 K, and unit concentrations of O_2 and Fe, with the O_2 concentration being kept constant. Also, the reduction potential of the metal species (E_M) is set to be 0.771 V *vs.* SHE, that of $Fe^{2+/3+}$ in water. In practical systems, Fe^{2+} is the most likely metal ion to serve as electron source for ROS generation, given that the walls of the absorber are composed of Fe alloy. These relations allow us to calculate the equilibrium concentrations of each ROS while accounting for the effect of dissolved metal concentration, as illustrated in Fig. 1(b). In acidic conditions (pH < 7), H_2O_2 and $^{\bullet}OH$ are the dominant species as expected, with their concentrations decreasing as the solution becomes more alkaline. At pH = 6 and pH = 3, the respective concentrations of H_2O_2 and $^{\bullet}OH$ become equal to that of O_2^-. In a moderately alkaline system (pH = 10), the concentration of $^{\bullet}OH$ is negligible, while H_2O_2 is almost 10 orders of magnitude smaller than O_2^-. This analysis clearly demonstrates that O_2^- is most likely the dominant ROS at equilibrium in an aqueous amine solution, where pH typically ranges from 8 to 14.[5] We note that O_2^- rather than $^{\bullet}OH$ explains the dominance of a few products in oxidative degradation.[5] The latter is much more reactive and therefore has a much shorter lifetime and,[34] meaning a great diversity of products would be expected if $^{\bullet}OH$ were the dominant ROS.

3.2. Effect of metal cation ligand environment

By eqn (4), the concentrations of ROS at equilibrium are a function of $[O_2]$, [M], T, pH and E_M. At a reduction potential of 0.771 V *vs.* SHE, the total concentration of ROS is miniscule (10^{-6} to 10^{-9} M) regardless of the other parameters. The half-cell potential of the Fe^{2+}/Fe^{3+} redox couple in pure aqueous media is too positive to reduce substantial amounts of O_2, let alone form $^{\bullet}OH$. Fig. 2 plots the equilibrium concentrations of ROS as a function of E_M at a pH of 10. Decreasing E_M (making the complex more reductive) results in large increases in concentrations for all ROS species with O_2^- predominating over the later-stage products (H_2O_2 and $^{\bullet}OH$) until −0.1 V *vs.* SHE. In the presence of such highly reductive metal complexes, $^{\bullet}OH$ can be produced in greater quantity than O_2^-, although such high energy complexes are unlikely to exist in large quantities. The more likely case is that an appreciable amount of moderate potential complexes produces O_2^- as the main ROS.

With the dominance of O_2^- shown, the only unknown remaining is the identity of the moderately reductive metal complexes. While the $Cu^{1+/2+}$ couple in aqueous media fits

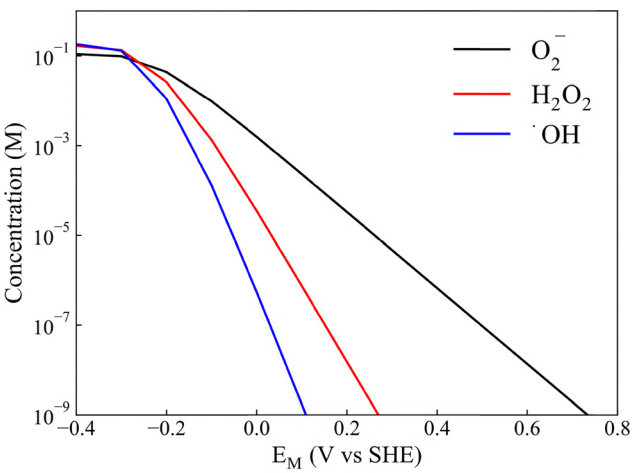

Fig. 2 Equilibrium concentrations of ROS at pH = 10 as a function of Fe complex reduction potential.

within the moderate potential region, Fe is overwhelmingly more abundant in the tank walls. This leads us to speculate that some Fe species exist with electronic structures more favorable to oxidation than the pure aqueous case.

The 3d electrons of octahedral Fe^{2+} complexes are split into the non-bonding t_{2g} set and the anti-bonding e_{g^*} set by σ-bonding with the surrounding ligands. The oxidation of Fe^{2+} requires the removal of an electron from the lower energy t_{2g} set to preserve the net spin, as removal from the e_{g^*} set would change the net spin, making the transition spin-forbidden. The energy difference between the t_{2g} set and the semi-occupied HOMO of O_2 is the equilibrium potential of (R1), denoted by ΔE.

The right portion of Fig. 3 illustrates the effect of substituting a water ligand with a ligand with free p-orbitals, denoted as the π ligand. In this case, the interaction between the t_{2g} orbitals of Fe^{2+} and the filled non-bonding p-orbitals of the π ligand interact splitting the normally non-bonding t_{2g} set into bonding t_{2g} and anti-bonding t_{2g^*}. The electron is now drawn from these anti-bonding t_{2g^*} orbitals when oxidation occurs. The energy increase of these anti-bonding t_{2g^*} orbitals directly corresponds to a decrease in reduction potential (ΔE_π), making O_2 reduction more thermodynamically favorable.

In a CO_2-loaded amine solution, the available species to serve as π ligands are OH^-, HCO_3^- and amine carbamate, with the latter two species being formed exclusively from CO_2 absorption. To quantify the effect of these species on electron transfer, we calculated the equilibrium potential of the $Fe^{2+/3+}$ couple in various ligand environments.

Table 1 lists the calculated equilibrium potentials of the $Fe^{2+/3+}$ couple when a single water in an octahedral complex is exchanged for one of the ligands (L = OH^-, HCO_3^-, or $MEACOO^-$). The minimum energy electron configuration is a high spin $t_{2g}^4 e_{g^*}^2$ state for all complexes analyzed here. Note that our calculated potential for the fully aqueous complex $[Fe(H_2O)_6]$ deviates by only 0.006 V from the experimental value, demonstrating a high accuracy of our calculations.

Table 1 Reduction potentials after a single ligand (L) substitution

Structure formula $Fe^{2+}(H_2O)_5L$, L =	E^0 [V]
H_2O	0.765
OH^-	0.211
HCO_3^-	0.203
$MEACOO^-$	0.226

As summarized in Table 1, substitution of a single H_2O for any π ligand in the $Fe^{2+}(H_2O)_6$ complex results in about 0.5 V more favorable reduction potential, indicating that ligand (L) substitution enhances the ability of Fe complex to reduce O_2. The donation effect illustrated in Fig. 3 is further corroborated by comparing the densities of states (DOS) of each complex as shown in Fig. S1. The modified complexes show a shift higher in energy of the frontier orbitals (located just below −5 eV *vs.* vacuum), indicative of higher energy (more reductive) electrons. Furthermore, charge decomposition analysis of the $MEACOO^-$ complex (see Fig. S2) reveals that ligand orbitals contribute significantly to the elevation of the Fe frontier molecular orbitals.[35,36]

Thermodynamically, the energy required to oxidize the Fe^{2+} ion decreases due to the complex becoming less stable in its reduced form. To reach such an elevated state, a driving force is required for substitution. Considering that the concentration of OH^- is small at realistic pH, only 10^{-4} at pH = 10 for example, OH^- substitution is unlikely to occur. On the other hand, the concentration of HCO_3^-/$MEACOO^-$ can exceed several molar. The large concentration of such ligands can provide the necessary driving force to produce an appreciable number of substituted complexes. In essence, large concentrations of HCO_3^-/$MEACOO^-$ shift the mean ligand environment of Fe^{2+} cations towards a more reductive potential. In this way, these complexes

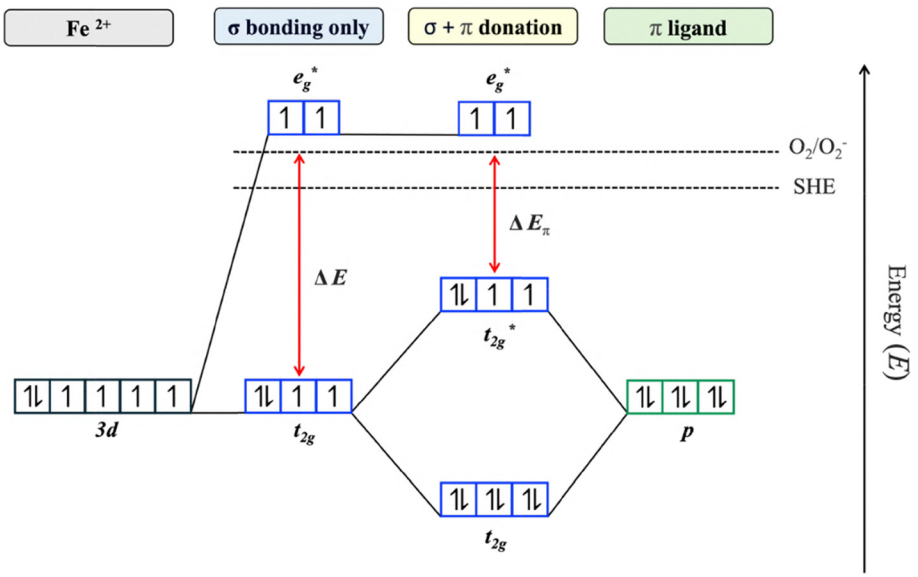

Fig. 3 Molecular orbital diagram of π-donation increasing electron energy and decreasing reduction potential.

can transfer an appreciable quantity of electrons to O_2, producing ROS (O_2^-) and causing oxidative degradation. Indeed, experiments have shown increased rates of oxidative degradation in CO_2-loaded solutions compared to unloaded solutions.[5]

For completeness, we have also computed reduction potentials for di-substituted complexes, which are presented in Table S2. Further substitution results in a compounding of the ligand effect, shifting the reduction potential to negative values *vs.* SHE. However, these complexes are rather unlikely to form considering the concentration of Fe complexes and the inherent energy cost associated with forming such a reductive complex.

3.3. Role of superoxide in oxidative degradation initiation

We now consider the reaction of O_2^- with protonated MEA ($MEAH^+$) to produce NH_3, one of the dominant degradation products.[5] CO_2 absorption into an aqueous MEA solution occurs through the $2MEA + CO_2 \rightarrow MEACOO^- + MEAH^+$ reaction. The protonation of N in MEA induces charge redistribution, withdrawing electron density from the adjacent alpha-C (C_α). As depicted in Fig. 4, O_2^- can act as a nucleophile to attack the electrophilic C_α in $MEAH^+$, accompanied by the release of NH_3, *i.e.*, $MEAH^+ + O_2^- \rightarrow HOCH_2C_\alpha H_2OO^\bullet + NH_3$. The reactive intermediate, $HOCH_2C_\alpha H_2OO^\bullet$, may undergo further reactions, leading to the formation of experimentally-observed single-carbon products such as formaldehyde and formic acid.[37]

We first used a static dimer method transition-state search with an implicit solvent model to evaluate the enthalpic barrier for the reaction of O_2^- with $MEAH^+$. As shown in Fig. 5, in the transition state (TS), the C_α of MEA becomes a trigonal bipyramidal five-coordinate center with NH_3 and –OO in the polar positions. The N–C_α–O angle is 162°, close to the idealized linear arrangement; this is a characteristic of an SN_2 reaction where the formation of the C_α–O bond and the breaking of the C_α–N bond occur simultaneously. The C_α–O–O angle, 116°, indicates a nucleophilic attack by the frontier orbitals of O_2^-, which are skewed relative to the O–O axis. The partial charges on all states in this calculation are denoted in Table S4. The trend from initial to final state is indicative of a charge transfer from the bottom O to N, as expected in the formation of NH_3 from a protonated amine. The enthalpic barrier, representing the energy difference, without entropy, between this TS complex and the reactants, is predicted to be 21.7 kcal mol^{-1}.

We also conducted well-tempered metadynamics simulations using an explicit solvent model to evaluate the free energy barrier while accounting entropic contributions at finite temperatures. $30H_2O$, 1 $MEAH^+$, and $1O_2^-$ molecules are placed in a cubic simulation box with an edge length of 9.5 Å and periodic boundary conditions, corresponding to about 10 wt% of MEA solution. The system was equilibrated for 5 ps, confirming the stable presence of $MEAH^+$ and O_2^-. As shown in

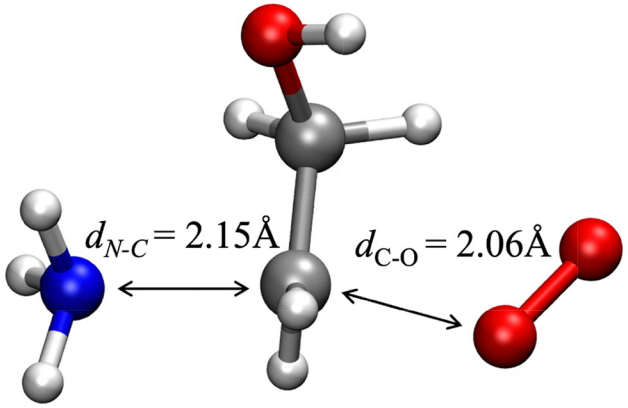

Fig. 5 The transition state geometry of the O_2^- attack on the C_α of $MEAH^+$ obtained from the dimer method. Blue, grey, red, and white balls represent N, C, O, and H respectively.

Fig. 6, a single collective variable (CV) of $d_{C\text{–}OO} - d_{C\text{–}N}$ was employed to mimic the SN_2 reaction involving simultaneous C_α–O bond formation and C_α–N bond cleavage. For further verification, we also conducted metadynamics simulations using 2 CVs, $d_{C\text{–}OO}$ and $d_{C\text{–}NH_3}$, as shown in Fig. S5. In our simulations, the formation of the C–OO bond was always accompanied by a simultaneous breaking of the C–N bond. Moreover, the observed TS geometries closely resemble the TS structure from static calculations in Fig. 6.

The free-energy barrier is predicted to be 28.9 kcal mol^{-1} at 313 K, which is greater than the enthalpy barrier of 21.7 kcal mol^{-1}. The difference is primarily attributed to the solvation effect of O_2^-.

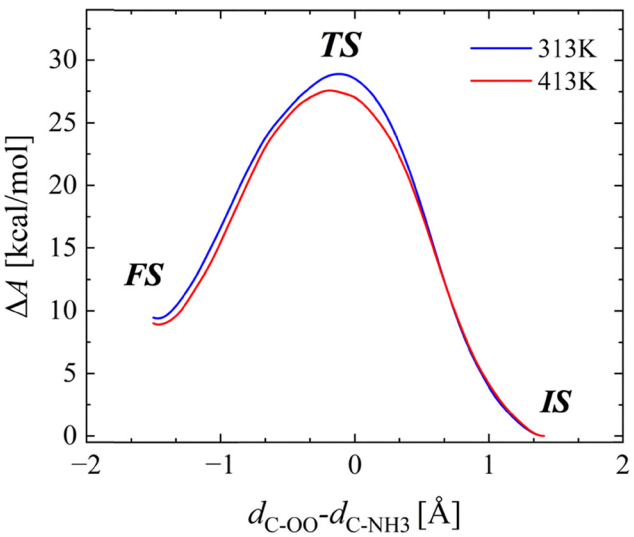

Fig. 6 Free-energy profile of the reaction in Fig. 5 at T = 313 K and T = 413 K. IS = initial state, TS = transition state, FS = final state.

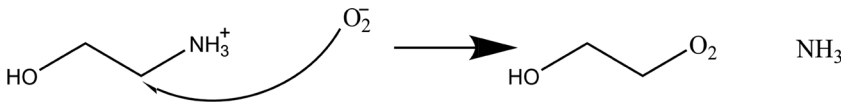

Fig. 4 The proposed mechanism of O_2^- initiating MEA degradation.

The free-energy barrier may decrease with increasing temperature, as the solvent effect diminishes (see Fig. S8); that is, as the temperature increases, water molecules solvating O_2^- become more mobile and less rigidly organized, thereby facilitating the intermolecular reaction.[38] Given the relatively moderate barriers, our work highlights that O_2^-, the most likely ROS, can play a key role in initiating the oxidative degradation of aqueous MEA solvents, especially in CO_2 stripping conditions.

4. Conclusions

We investigated the generation of ROS and the role of metal complexes in typical CO_2 capture processes using a combination of thermodynamic analysis and static QM calculations. Our findings clearly identify the predominant ROS in aqueous amine solutions, with a focus on the role of Fe^{2+} complexes and effect of CO_2-derived products as ligands. The key findings are summarized as follows:

• Our thermodynamic analysis demonstrates that $^{\bullet}OH$ and H_2O_2 may be dominant in environments with plentiful protons and electrons. However, under typical CO_2 capture conditions, O_2^- is likely to be the dominant ROS. considering the small quantity of metal cations and its alkaline environment.

• The substitution of a water ligand in $Fe(H_2O)_6$ with π ligands, such as OH^-, HCO_3^-, and $MEACOO^-$, can significantly lower the reduction potential by π-backdonation. Also, CO_2-loaded solutions, where concentrations of HCO_3^- and $MEACOO^-$ are relatively high and act as ligands in Fe complex, enables the formation of a considerable amount of O_2^-.

• Our free-energy barrier calculations suggest that oxidative degradation of MEA can be initiated by the attack of O_2^- on the electrophilic C_α of protonated MEA ($MEAH^+$), accompanied by the release of NH_3 *via* SN_2 mechanism.

We emphasize that while other pathways could be proposed, the mechanism here importantly identifies O_2^- as the initiator of oxidative degradation, which is more reasonable based on our analysis than $^{\bullet}OH$. Our work suggests that this mechanism not only has implications for amine-based CO_2-capture but in other cases of ROS-related organic molecule degradation such as biological systems, where Fe^{2+} in alkaline conditions produces ROS which cause oxidative damage to proteins.[39]

Conflicts of interest

There are no conflicts to declare.

Data availability

The data supporting this study can be shared upon reasonable request.

Supplementary information including further discussion of the system of equations parameters and addtional metadynamics results. See DOI: **https://doi.org/10.1039/d5cp02617b**.

Acknowledgements

The authors would like to thank the Texas Advanced Computing Center (TACC) for providing the computational resources for these calculations.

References

1 M. Bui, C. S. Adjiman, A. Bardow, E. J. Anthony, A. Boston, S. Brown, P. S. Fennell, S. Fuss, A. Galindo, L. A. Hackett, J. P. Hallett, H. J. Herzog, G. Jackson, J. Kemper, S. Krevor, G. C. Maitland, M. Matuszewski, I. S. Metcalfe, C. Petit, G. Puxty, J. Reimer, D. M. Reiner, E. S. Rubin, S. A. Scott, N. Shah, B. Smit, J. P. M. Trusler, P. Webley, J. Wilcox and N. Mac Dowell, *Energy Environ. Sci.*, 2018, **11**, 1062–1176.
2 S. A. Bedell, *Energy Procedia*, 2009, **1**, 771–778.
3 H. Lepaumier, D. Picq and P.-L. Carrette, *Ind. Eng. Chem. Res.*, 2009, **48**, 9068–9075.
4 S. B. Fredriksen and K.-J. Jens, *Energy Proc.*, 2013, **37**, 1770–1777.
5 S. Chi and G. T. Rochelle, *Ind. Eng. Chem. Res.*, 2002, **41**, 4178–4186.
6 G. T. Rochelle, *Science*, 2009, **325**, 1652–1654.
7 M. J. Frisch, G. W. Trucks, H. B. Schlegel, G. E. Scuseria, M. A. Robb, J. R. Cheeseman, G. Scalmani, V. Barone, G. A. Petersson, H. Nakatsuji, X. Li, M. Caricato, A. V. Marenich, J. Bloino, B. G. Janesko, R. Gomperts, B. Mennucci, H. P. Hratchian, J. V. Ortiz, A. F. Izmaylov, J. L. Sonnenberg, D. Williams-Young, F. Ding, F. Lipparini, F. Egidi, J. Goings, B. Peng, A. Petrone, T. Henderson, D. Ranasinghe, V. G. Zakrzewski, J. Gao, N. Rega, G. Zheng, W. Liang, M. Hada, M. Ehara, K. Toyota, R. Fukuda, J. Hasegawa, M. Ishida, T. Nakajima, Y. Honda, O. Kitao, H. Nakai, T. Vreven, K. Throssell, J. A. Montgomery, Jr., J. E. Peralta, F. Ogliaro, M. J. Bearpark, J. J. Heyd, E. N. Brothers, K. N. Kudin, V. N. Staroverov, T. A. Keith, R. Kobayashi, J. Normand, K. Raghavachari, A. P. Rendell, J. C. Burant, S. S. Iyengar, J. Tomasi, M. Cossi, J. M. Millam, M. Klene, C. Adamo, R. Cammi, J. W. Ochterski, R. L. Martin, K. Morokuma, O. Farkas, J. B. Foresman and D. J. Fox, *Gaussian 16 Rev. C.01*, 2016.
8 A. D. Becke, *J. Chem. Phys.*, 1993, **98**, 5648–5652.
9 Y. Zhao and D. G. Truhlar, *Theor. Chem. Acc.*, 2008, **120**, 215–241.
10 A. V. Marenich, C. J. Cramer and D. G. Truhlar, *J. Phys. Chem. B*, 2009, **113**, 6378–6396.
11 A. L. Orjuela, F. Núñez-Zarur and J. Alí-Torres, *RSC Adv.*, 2022, **12**, 24077–24087.
12 T. Yanai, D. P. Tew and N. C. Handy, *Chem. Phys. Lett.*, 2004, **393**, 51–57.
13 R. Car and M. Parrinello, *Phys. Rev. Lett.*, 1985, **55**, 2471–2474.
14 A. D. Becke, *Phys. Rev. A: At., Mol., Opt. Phys.*, 1988, **38**, 3098–3100.
15 C. Lee, W. Yang and R. G. Parr, *Phys. Rev. B: Condens. Matter Mater. Phys.*, 1988, **37**, 785–789.

16 L. Lespade, *Chem. Phys.*, 2016, **475**, 32–38.
17 J. Li, H. Hou and B. Wang, *J. Phys. Chem. A*, 2009, **113**, 800–804.
18 N. Troullier and J. L. Martins, *Phys. Rev. B: Condens. Matter Mater. Phys.*, 1991, **43**, 1993–2006.
19 L. Kleinman and D. M. Bylander, *Phys. Rev. Lett.*, 1982, **48**, 1425–1428.
20 S. Nosé, *J. Chem. Phys.*, 1984, **81**, 511–519.
21 W. G. Hoover, *Phys. Rev. A: At., Mol., Opt. Phys.*, 1985, **31**, 1695–1697.
22 G. J. Martyna, M. L. Klein and M. Tuckerman, *J. Chem. Phys.*, 1992, **97**, 2635–2643.
23 M. Bonomi, D. Branduardi, G. Bussi, C. Camilloni, D. Provasi, P. Raiteri, D. Donadio, F. Marinelli, F. Pietrucci, R. A. Broglia and M. Parrinello, *Comput. Phys. Commun.*, 2009, **180**, 1961–1972.
24 A. Laio and M. Parrinello, *Proc. Natl. Acad. Sci. U. S. A.*, 2002, **99**, 12562–12566.
25 A. Barducci, G. Bussi and M. Parrinello, *Phys. Rev. Lett.*, 2008, **100**, 020603.
26 R. Gowers, M. Linke, J. Barnoud, T. Reddy, M. Melo, S. Seyler, J. Domański, D. Dotson, S. Buchoux, I. Kenney and O. Beckstein, *MDAnalysis: A Python Package for the Rapid Analysis of Molecular Dynamics Simulations*, Austin, Texas, 2016, pp. 98–105.
27 N. Michaud-Agrawal, E. J. Denning, T. B. Woolf and O. Beckstein, *J. Comput. Chem.*, 2011, **32**, 2319–2327.
28 P. Smith, R. M. Ziolek, E. Gazzarrini, D. M. Owen and C. D. Lorenz, *Phys. Chem. Chem. Phys.*, 2019, **21**, 9845–9857.
29 G. Kresse and J. Furthmüller, *Phys. Rev. B: Condens. Matter Mater. Phys.*, 1996, **54**, 11169–11186.
30 G. Henkelman and H. Jónsson, *J. Chem. Phys.*, 1999, **111**, 7010–7022.
31 J. P. Perdew, K. Burke and M. Ernzerhof, *Phys. Rev. Lett.*, 1996, **77**, 3865–3868.
32 G. Kresse and D. Joubert, *Phys. Rev. B: Condens. Matter Mater. Phys.*, 1999, **59**, 1758–1775.
33 K. Krumova and G. Cosa, in *Singlet Oxygen: Applications in Biosciences and Nanosciences*, ed. S. Nonell, C. Flors, S. Nonell and C. Flors, The Royal Society of Chemistry, 2016.
34 J. M. Burns, W. J. Cooper, J. L. Ferry, D. W. King, B. P. DiMento, K. McNeill, C. J. Miller, W. L. Miller, B. M. Peake, S. A. Rusak, A. L. Rose and T. D. Waite, *Aquat. Sci.*, 2012, **74**, 683–734.
35 T. Lu and F. Chen, *J. Comput. Chem.*, 2012, **33**, 580–592.
36 X. Meng and T. Lu, *J. Adv. Phys. Chem.*, 2015, **04**, 111–124.
37 J. Yu, D. Patel and G. S. Hwang, *Ind. Eng. Chem. Res.*, 2025, **64**, 15505–15511.
38 P. Han and D. M. Bartels, *J. Phys. Chem.*, 1996, **100**, 5597–5602.
39 V. I. Lushchak, *Biochemistry*, 2007, **72**, 809–827.